Structural and electronic properties of rare-earth chromites: A computational and experimental study

Jianhang Shi, Gayanath W. Fernando, Yanliu Dang, Steven L. Suib, and Menka Jain

Phys. Rev. B **106**, 165117 — Published 18 October 2022

DOI: 10.1103/PhysRevB.106.165117

Structural and electronic properties of rare-earth chromites: A computational and experimental study

Jianhang Shi,[1,2] Gayanath W. Fernando,[3] Yanliu Dang,[2] Steven L. Suib,[2,4] and Menka Jain[2,3]

[1]*Department of Materials Science and Engineering, University of Connecticut, Storrs, CT 06269, USA*

[2]*Institute of Materials Science, University of Connecticut, Storrs, CT 06269, USA*

[3]*Department of Physics, University of Connecticut, Storrs, CT 06269, USA*

[4]*Department of Chemistry, University of Connecticut, Storrs, CT 06269, USA*

Abstract: In this work, the structural, optical, and electronic properties of rare-earth perovskites of the general formula $RCrO_3$, where R represents the rare-earth Gd, Tb, Dy, Ho, Er, and Tm, have been studied in detail. These compounds were synthesized through a facile citrate route. X-ray diffraction, Raman spectroscopy, and UV-Vis spectroscopy were used to reveal the structural evolutions in $RCrO_3$. The lattice parameter, Cr^{3+}-O^{2-}-Cr^{3+} bond angle, and CrO_6 octahedral distortions were found to strongly depend on the ionic radii of the rare-earth element. First-principles calculations based on density-functional theory within the generalized gradient approximation (GGA) of Perdew- Burke- Ernzerhof (PBE) and strongly constrained-and-appropriately normed (SCAN) meta-GGA were also employed to calculate the structural and electronic properties of $RCrO_3$. The ground-state energy, lattice constants, electronic structure, and density of states (DOS) of $RCrO_3$ were calculated. These provide some insights into the electronic characteristics of the series of $RCrO_3$ compounds. The calculated values of lattice parameters and bandgaps with Hubbard U correction (SCAN+U) agree well with values measured experimentally and show more accuracy in predicting the ground-state crystal structure and band structure compared to PBE+U approximation. The bandgap of $RCrO_3$ is found to be independent of the ionic radii of the element R from both experiments and calculations.

1. Introduction

Oxides consisting of rare-earth element (R) with partially occupied $4f$ shell are crucial in modern technologies due to their various intriguing magnetic, luminescent, and electrochemical properties for potential applications as multifunctional materials.[1,2] Investigations on oxides, such as rare-earth orthoferrites ($RFeO_3$),[3-5] manganites ($RMnO_3$),[6-8] nickelates ($RNiO_3$),[9-11] and orthochromites ($RCrO_3$),[12-14] have provided remarkable opportunities to enhance our understanding of the relationships between structural and physical properties.[15] Among the rare-earth oxides, the $RCrO_3$ with a distorted perovskite structure exhibiting unique interesting properties, such as spin reorientation, magnetization reversal, and large magnetocaloric effect, are currently attracting increasing research interest.[15] The $RCrO_3$ family of materials have shown to exhibit a G-type canted anti-ferromagnetism below *Néel* temperature, T_N^{Cr}, where the Cr^{3+} spin orders.[16] The canting is presumed to be the source of weak ferromagnetism, which is the result of antisymmetric Dzyaloshinskii-Moriya (DM) interaction.[17] The transition temperatures (T_N^{Cr}) have been reported to shift to higher values with the increasing R-ion ionic radii, which could be attributed to the decreasing of lattice distortions and increasing $Cr^{3+}– O^{2-}– Cr^{3+}$ bond angles.[18] Recently, some of the rare-earth chromites were reported to be magnetoelectric multiferroics due to the coexistence of electric and magnetic orders, such as in $GdCrO_3$.[19] These properties allow $RCrO_3$ for possible practical applications such as spin-injection devices and nonvolatile magnetic random access memories. For periodic solids, first attention by the computational solid-state community goes towards predicting the fundamental bandgap of materials due to its relevance in technological applications, such as opto-electronics and photovoltaics. $RCrO_3$ materials have also been studied as optically active photo catalyst due to the presence of slightly distorted CrO_6 octahedral complex.[17] Some materials of the $RCrO_3$ family have been reported to have wide bandgap with a value ranging from 2.19 to 3.20 eV based on the results obtained from the UV–Visible spectroscopy.[17]

Theoretically, first-principles computational techniques based on density functional theory (DFT) provide an extremely valuable tool for predicting stable structures and energetics of materials for both finite and periodic systems.[20] Several approximations have been developed to allow for calculations at various levels of accuracy, such as generalized gradient approximation (GGA) in a standard form of Perdew-Burke-Ernzerhof (PBE) and meta-GGA in the form of the

Strongly Constrained and Appropriately Normed (SCAN) functional.[21] However, these approximations could sometimes dramatically underestimate the bandgaps (E_g) for strongly correlated systems or insulators due to the existence of a derivative discontinuity of the energy with respect to the number of electrons or the use of a local potential to represent exchange.[22-24] For rare-earth compounds, the *f*- and *d*-orbital correlations are also important when and where some atomic character of the orbitals survive, and spin-orbit effects are strong. The local-density approximation (LDA+U) type schemes were developed in the context of Mott-Hubbard insulators and are applicable in cases such as the *f*-electron systems where the atomic orbital character (as opposed to the itinerant character) survives to an appreciable degree. This is of course an approximate way to deal with strong correlations. In such cases, The accuracy of the DFT approximations is improved by incorporating a Hubbard-model-type correction (+U, correction to approximate DFT functionals such as, e.g., LDA, GGA, or meta-GGA), in which an empirical on-site potential (U) is added to the atomic pseudo-potential to account for localized *d* and *f* orbitals.[25] For many magnetoelectric multiferroic materials, such as $TbMnO_3$, $HoMnO_3$, etc., the first-principles results have been shown to be very sensitive to the choice of the on-site potential.[26] We note that spin-polarized versions of such density functionals have to be implemented when studying magnetic materials.

There are only a few reports on the standard calculations of the $RCrO_3$ based on DFT to understand the band structure. For example, Terkhi *et al.* reported a bandgap of 2.15 eV of $GdCrO_3$ calculated by the modified Becke–Johnson (mBJ) exchange potential using the WIEN2K code,[27] which is lower than experimentally observed value of 3.15 eV.[17] Terkhi *et al.* also demonstrated the bandgap of $NdCrO_3$ underestimated by GGA-PBE could be more accurately predicted by GGA plus Tran–Blaha-modified Becke–Johnson scheme.[28] For $DyCrO_3$, bandgap was calculated to be 2.7 eV where for the exchange and correlation energy, the PBE functional under GGA was employed via Vienna *ab initio* simulation package (VASP), which is also lower than its experimentally observed value of 3.19 eV.[17,29] This bandgap of 2.7 eV is attributed to the charge transfer gap between O 2*p* and Cr 3*d* states. In the work by Ong *et al.*, three optical gaps were identified: a charge transfer gap of 3.40 eV, a gap of 2.15 eV responsible for its green color, and an energy bandgap of 1.40 eV between the occupied Cr t_{2g} and unoccupied Cr e_g orbitals.[30] However, in case of pure $LaCrO_3$, the bandgap of 2.15 eV is not revealed by the reflectivity measurement that would make it a colorless material, which is in contradiction to its observed light green color. Although the aforementioned efforts have been made, the electronic structure of some $RCrO_3$ compounds remain to be well-understood from a theoretical point of view. Theoretical work in this direction can lead to useful insights of the underlying physics of the evolution of their electronic structure and provide crucial information that can lead to the design of materials with enhanced physical properties, such as multiferroic behavior in the $RCrO_3$ family of materials.

In this article, we report experimental and theoretical investigations of the structural and electronic properties in the $RCrO_3$ family of materials (R = Gd, Tb, Dy, Ho, Er, and Tm) synthesized via a solution route. The experimentally observed optical bandgap of ~ 3.3 eV is found to be related to the transitions between the O 2*p* valence band and the bottom of the conduction band. DFT based calculations are performed within a collinear arrangement of R^{3+} and Cr^{3+} spins where the two exchange-correlation functionals were used within VASP: (PBE) GGA and (SCAN) meta-GGA functionals. The on-site Coulomb interaction correction was applied to both functionals, which after correction are called as PBE+U and SCAN+U methods. To our knowledge, this is the first systematic experimental and theoretical study in the $RCrO_3$ material for determining relations between the structural modulation and electronic properties.

2. Experimental and computational details

The bulk powder samples of $RCrO_3$ (R = Gd, Tb, Dy, Ho, Er, and Tm) were synthesized by a citrate solution route. For this, high purity (> 99.99%) nitrate salts were obtained from Alfa Aesar. At first, the metal salts were dissolved in water stoichiometrically and then mixed together with citric acid. The obtained solution was continuously stirred, heated, and dried on a hot plate. The resultant powder was then grinded in mortar pestle and annealed at 900 °C for 2 h in oxygen atmosphere to obtain $GdCrO_3$ (GCO), $TbCrO_3$ (TbCO), $DyCrO_3$ (DCO), $HoCrO_3$ (HCO), $ErCrO_3$ (ECO), and $TmCrO_3$ (TmCO) bulk powder samples. The crystal structure of these powder samples was examined by X-ray diffraction (XRD, Bruker D2 Phaser diffractometer with Cu-Kα radiation) and by Raman spectroscopy (Renishaw System 2000 using 514 nm Ar-ion laser) techniques. The UV–Vis spectra of the samples were recorded using Shimadzu UV-2450 UV-Vis Spectrometer in a range of 200–800 nm using deuterium and halogens.

DFT-based spin-polarized electronic-structure calculations were carried out using projector-augmented wave method as implemented in VASP,[31,32] with a kinetic energy cutoff of 520 eV and a total energy convergence threshold of 10^{-6} eV.[29] In this work, the exchange correlation interaction is treated within the GGA using the PBE functional and within the meta-GGA using the SCAN functional, both with on-site Coulomb interactions (PBE+U, SCAN+U) for a better treatment of *3d* (Cr^{3+}) and *4f* (R^{3+}) electrons.[33] The structural properties and band structure of $RCrO_3$ are investigated here using PBE+U and SCAN+U and the two results are compared. The on-site Coulomb interaction presented in 3*d* states of the transitions metal-ion is corrected by the DFT+U (U is the Hubbard energy) method and the U value was set as 3 eV for Cr 3*d* states, in line with previous works.[20,28] The Hubbard U values for Gd, Tb, Dy, Ho, Er, and Tm were taken as 4.6, 5.0, 5.0, 4.9, 4.2, and 4.8 eV , respectively, according to the work by Topsakal *et al*.[34] We assume a 3+ oxidation state of rare-earth with *4f* electrons either frozen in the ionic core or included as valence electrons. The spin–orbit coupling and non-collinear magnetic states are not considered in these calculations. A 10 × 10 × 7 Γ-centered k-point mesh was used to sample the Brillouin zone corresponding to the 20-atom orthorhombic cell. The structures were fully relaxed until the forces acting on the atoms were smaller than 0.005 eV/Å.

3. Results and discussion

3.1 Spin configuration

Three types of antiferromagnetic spin structures are possible for R^{3+}/Cr^{3+} spins: G-AFM, C-AFM, and A-AFM.[35] Following the experimental evidence that the G-type spin structure is observed for both R^{3+} and Cr^{3+} sublattices from neutron elastic scattering measurements, the G-AFM spin arrangement is considered for both Cr^{3+} and R^{3+} moments in this work to save computation time.[35] Two typical spin configurations are proposed in the simulations: (i) R^{3+} cations were treated as non-magnetic with the 4*f* electrons frozen at the ionic core in simulations with PBE+U and (ii) R^{3+} cations were allowed to order magnetically with the 4*f* electrons treated as valence electrons in simulations with SCAN+U. The two spin configurations for Cr^{3+} and R^{3+} sublattice were initialized in G-AFM order in a 20-atom unit cell as shown in Fig. 1. A full structural relaxation with the R^{3+} and Cr^{3+} magnetic moments initialized was conducted within a self-consistent field calculation of the electronic structure. The resulting ground-state configuration is analyzed focusing on the ground-state band structure, magnetic moments, and structural parameters.

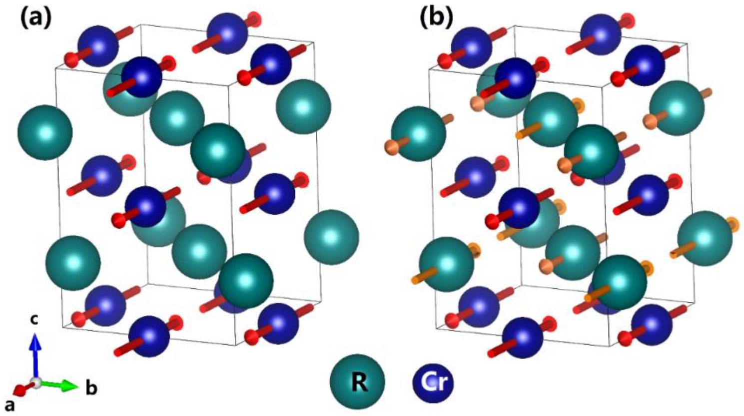

Figure 1. Spin configurations of R^{3+} and Cr^{3+} ions in $RCrO_3$ with: (a) R^{3+} treated as non-magnetic ion with 4*f* electrons frozen at the ionic core for the PBE+U and (b) R^{3+} treated as magnetic ion with 4*f* electrons solved explicitly for the SCAN+U.

Tables 1 and 2 summarize the ground state magnetic moments of ions in a representative material $GdCrO_3$ in $RCrO_3$, which was optimized by the PBE+U and SCAN+U simulations, respectively. In these tables, the contributions to the total (spin) magnetic moments of *s*, *p*, *d*, and *f* electrons are listed. It is observed that the major contribution to total magnetic moments is from electrons of *d* and *f* shells for Cr^{3+} and Gd^{3+}, respectively. The calculations predict that both Gd^{3+} and Cr^{3+} sublattice moments align antiferromagnetically in a collinear fashion. A zero net total moment of $GdCrO_3$ is observed in the present PBE+U and SCAN+U simulations. Similar results (negligible net total moments of $RCrO_3$) were reported in other rare-earth chromties in SCAN+U simulations, indicating the predominant antiferromagnetic spin configuration in $RCrO_3$ ground state.

Table 1. Details of the optimized magnetic moments in $GdCrO_3$ calculated by PBE+U. The atomic positions (*a*, *b*, *c*) of listed atoms are as follows: Gd (1): (0.982, 0.065, 0.250), Gd (2): (0.018, 0.935, 0.750), Gd (3): (0.482, 0.435, 0.750), Gd (4): (0.518, 0.565, 0.250), Cr (1): (0.500, 0, 0), Cr (2): (0, 0.500, 0), Cr (3): (0.500, 1.000, 0.500), Cr (4): (1.000, 0.500, 0.500).

Atom	***s*** **(μ_B)**	***p*** **(μ_B)**	***d*** **(μ_B)**	**Total moment (μ_B)**
Gd (1)	-0.00	-0.00	0.00	0.00
Gd (2)	0.00	0.00	-0.00	-0.00
Gd (3)	-0.00	-0.00	0.00	0.00
Gd (4)	0.00	0.00	-0.00	-0.00
Cr (1)	-0.02	-0.03	-2.87	-2.93
Cr (2)	0.02	0.03	2.87	2.93
Cr (3)	0.02	0.03	2.87	2.93
Cr (4)	-0.02	-0.03	-2.87	-2.93
Total	0.00	0.00	0.00	0.00

Table 2. Details of the optimized magnetic moments in $GdCrO_3$ calculated by SCAN+U. The atomic (*a*, *b*, *c*) positions of listed atoms are as follows: Gd (1): (0.982, 0.064, 0.250), Gd (2): (0.018, 0.936, 0.750), Gd (3): (0.482, 0.436, 0.750), Gd (4): (0.518, 0.564, 0.250), Cr (1): (0.500, 0, 0), Cr (2): (0, 0.500, 0), Cr (3): (0.500, 1.000, 0.500), Cr (4): (1.000, 0.500, 0.500).

Atom	***s*** **(μ_B)**	***p*** **(μ_B)**	***d*** **(μ_B)**	***f*** **(μ_B)**	**Total moment (μ_B)**
Gd (1)	-0.01	-0.03	0.10	7.01	7.08
Gd (2)	0.01	0.03	-0.10	-7.01	-7.08
Gd (3)	-0.01	-0.03	0.10	7.01	7.08
Gd (4)	0.01	0.03	-0.10	-7.01	-7.08
Cr (1)	-0.02	-0.03	-2.85	0.00	-2.90
Cr (2)	0.02	0.03	2.85	0.00	2.90
Cr (3)	0.02	0.03	2.85	0.00	2.90
Cr (4)	-0.02	-0.03	-2.85	0.00	-2.90
Total	0.00	0.00	0.00	0.00	0.00

3.2 Structural properties

The room temperature XRD patterns of the synthesized $RCrO_3$ (R = Gd, Tb, Dy, Ho, Er, and Tm) samples are presented in Fig. 2, with corresponding Miller indices (hkl) of the characteristic peaks.[15,36] All the peaks can be successfully indexed in the measured 2-Theta (2θ) range indicating that the samples are of single-phase with the space group *Pbnm* and polycrystalline in nature. Table 3 summarizes the 2θ positions of several representative peaks. The 2θ positions of most crystal planes were found to shift to higher 2θ angles as the rare-earth atom changes from Gd to Tm. In general, changes in the size of the ionic radius of an atom cause the 2θ angle shift and a change in diffraction intensity. The reduction in ionic radius of R^{3+} causes a 2θ angle to shift towards the right (larger angle values), which is in accordance with Bragg's Law (θ inversely proportional to the lattice parameter, where the lattice parameter is proportional to the ionic radius).This indicates systematic structural variation in the $RCrO_3$ series.

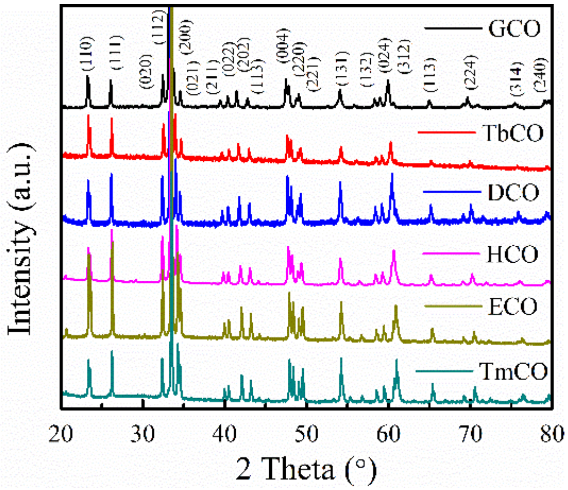

Figure 2. Room temperature X-ray diffraction (XRD) patterns of the bulk $RCrO_3$ (RCO).

Table 3. Experimentally obtained 2-theta positions of the (111), (112), (202), (220), and (312) planes in $RCrO_3$ compounds.

Sample	**(111)** (°)	**(112)** (°)	**(202)** (°)	**(220)** (°)	**(312)** (°)
GCO	26.091	33.232	41.446	47.495	59.977
TbCO	26.204	33.373	41.673	47.653	60.278
DCO	26.153	33.363	41.784	47.673	60.460
HCO	26.220	33.428	41.931	47.775	60.674
ECO	26.294	33.525	42.076	47.915	60.904
TmCO	26.254	33.505	42.086	47.935	61.015

The experimentally obtained XRD scans of all samples were fitted by using Rietveld refinements via FullProf Suite software assuming an orthorhombically distorted perovskite structure (space group *Pbnm*) and four formula units per unit cell. Useful structural information was extracted from the refinements and the obtained lattice parameters, bond angles, and unit cell volumes are summarized in the Table 4. The lattice parameters (*a* and *c*) and unit cell volume (V) were found to decrease with the decreasing ionic radii of R^{3+} (from Gd, Tb, Dy, Ho, Er, to Tm). The largest and smallest values of bond angles are observed in GCO and TmCO, respectively. In $RCrO_3$ with orthorhombically distorted structure, the decreasing values of the out-of-plane Cr-O_1-Cr and in-plane Cr-O_2-Cr bond angles (from an ideal 180 ° of ABO_3 cubic perovskites structure) that corresponds to the tilting of CrO_6 octahedral, leads to increasing distortion in the structure.[37] In the present work, the Cr-O_1-Cr and Cr-O_2-Cr bond angles were found to decrease with decreasing atomic number of rare-earths, which is consistent with the decreasing size of rare-earth cations.[15]

Table 4. Ionic radii (*r*) of rare-earth ions $RCrO_3$ (RCO) and structural parameters of various RCO compounds obtained by Rietveld refinement of the experimentally obtained XRD patterns: lattice parameters: *a*, *b*, *c*; unit cell volume: V; out-of-plane bond angle Cr-O_1-Cr, and in-plane bond angle Cr-O_2-Cr.

Sample	***r* (Å)**	***a* (Å)**	***b* (Å)**	***c* (Å)**	**V ($Å^3$)**	**Cr-O_1-Cr (°)**	**Cr-O_2-Cr (°)**
GCO	1.107	5.319	5.527	7.614	223.839	151.4	149.7
TbCO	1.095	5.298	5.523	7.584	221.870	146.6	147.4
DCO	1.083	5.270	5.526	7.562	220.193	146.5	150.5
HCO	1.072	5.252	5.529	7.550	219.202	145.9	148.4
ECO	1.062	5.229	5.521	7.526	217.275	144.8	144.6
TmCO	1.052	5.213	5.512	7.508	215.737	147.0	143.6

The relaxed lattice parameters were also calculated using DFT calculations. The Table 5 lists lattice parameters obtained using the initial spin configuration presented in Fig. 1(a) and PBE+U simulation, while Table 6 lists those using the spin configuration in Fig. 1(b) and SCAN+U simulation. Fig. 3 displays the experimental and computed parameters (Table 5 and Table 6) that indicated that the computed lattice parameters and unit cell volume depicts a trend that is consistent with those obtained experimentally. The Cr-O_1-Cr bond angle is found to be decreasing with reducing ionic radii of rare-earth using both PBE+U and SCAN+U simulations. It is evident from Fig. 3 that the SCAN+U predicted lattice parameters are in better agreement with the experimental results compared to the PBE+U simulation. This indicates that meta-GGA functional facilitates comparatively better calculation of the structural properties of $RCrO_3$ perovskites. This observation agrees with previous study in which the SCAN meta-GGA was shown to be superior to the PBE GGA for predicting the geometries and energies of diversely bonded materials (including metallic, ionic, hydrogen, covalent, and van der Waals bonds).[38]

Table 5. Structural parameters obtained from the DFT (PBE+U) simulations.

Sample	***a* (Å)**	***b* (Å)**	***c* (Å)**	**V (Å^3)**	**Cr-O_1-Cr (°)**	**Cr-O_2-Cr (°)**
GCO	5.340	5.614	7.679	230.246	145.60	146.66
TbCO	5.317	5.609	7.657	228.362	144.49	145.83
DCO	5.297	5.600	7.637	226.541	143.45	145.10
HCO	5.277	5.592	7.619	224.809	142.48	144.43
ECO	5.258	5.583	7.602	223.177	141.66	143.84
TmCO	5.237	5.569	7.582	221.147	140.59	143.12

Table 6. Structural parameters obtained from the DFT (SCAN+U) simulations.

Sample	***a* (Å)**	**b (Å)**	**c (Å)**	**V (Å^3)**	**Cr-O_1-Cr (°)**	**Cr-O_2-Cr (°)**
GCO	5.320	5.577	7.637	226.565	146.42	147.26
TbCO	5.284	5.555	7.592	222.857	144.24	145.69
DCO	5.262	5.525	7.570	220.074	142.92	144.44
HCO	5.224	5.517	7.538	217.223	141.56	143.47
ECO	5.241	5.535	7.548	218.939	142.08	143.95
TmCO	5.199	5.506	7.514	215.081	140.27	142.61

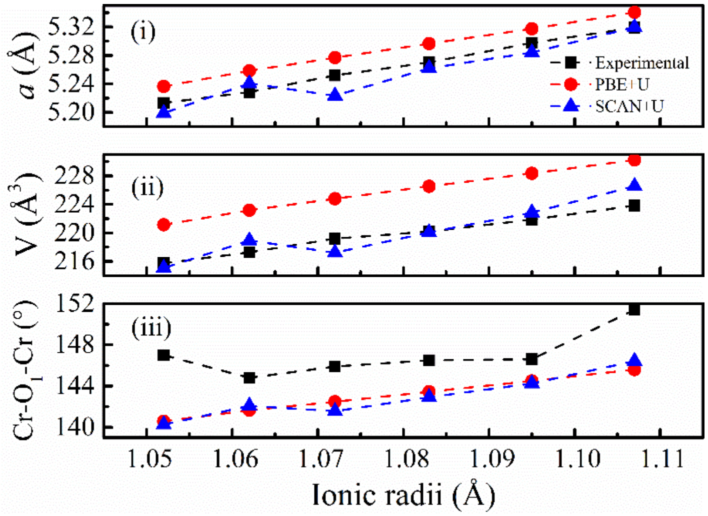

Figure 3. Comparison of (i) lattice parameter *a*, (ii) unit cell volume (V) and (iii) out-of-plane bond angle Cr-O_1-Cr obtained from DFT and Rietveld refinement of the experimental XRD data.

The $RCrO_3$ compounds with *Pbnm* space group contains four formula units per Bravais unit cell. Among 60 irreducible representation for vibration modes of atoms at four different Wyckoff sites, only 24 phonon modes ($7A_g + 7B_{1g} + 5B_{2g} + 5B_{3g}$) were reported to be Raman-active.[39] Several characteristic Raman modes out of those 24 were observed in the Raman spectra of present samples as shown in Fig. 4. In these, several modes merged to form a broad peak for some $RCrO_3$ samples.[40] The assignment of phonon modes to the chromite spectra were carried out according to the work by Weber *et al.* and Camara *et al*.[40,41] The Raman modes A_g (~140 cm^{-1}) and B_{2g} (~160 cm^{-1}) are induced by displacements of the R-site ions since the heaviest atom of the structure is anticipated to vibrate at the low wave number region.[40] Bands in mid-spectral region (200-400 cm^{-1}), such as A_g (~260 cm^{-1}), A_g (~330 cm^{-1}), and A_g (~400 cm^{-1}), are very sensitive to the changes in the orthorhombic distortion. Two modes $A_g(3)$ and $A_g(5)$ have been identified as octahedral rotation soft modes, as Raman shifts scale linearly with the tilt angle of the CrO_6 octahedra.[40] Both $A_g(3)$ and $A_g(5)$ are found to increase with the decreasing of the ionic radii of rare-earth, indicating a larger tilt angle [={180-(Cr-O_1-Cr)}/2] for $RCrO_3$ with smaller ionic radii. This observation agrees with the results predicted by the DFT-predicted bond angle in Fig. 3(iii). The experimentally obtained Raman shift of some modes for all samples are summarized in Table 7 and for some representative modes are plotted in Fig. 5 that depicts that Raman modes shifted to lower wave numbers with the increasing ionic radii.

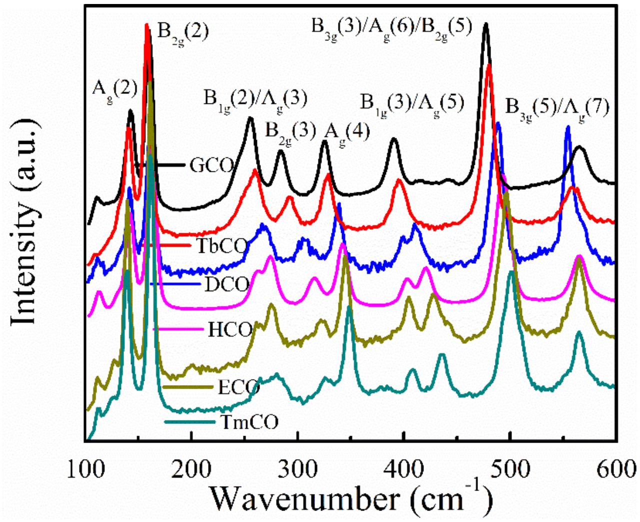

Figure 4. Room temperature Raman spectra of rare-earth chromites.

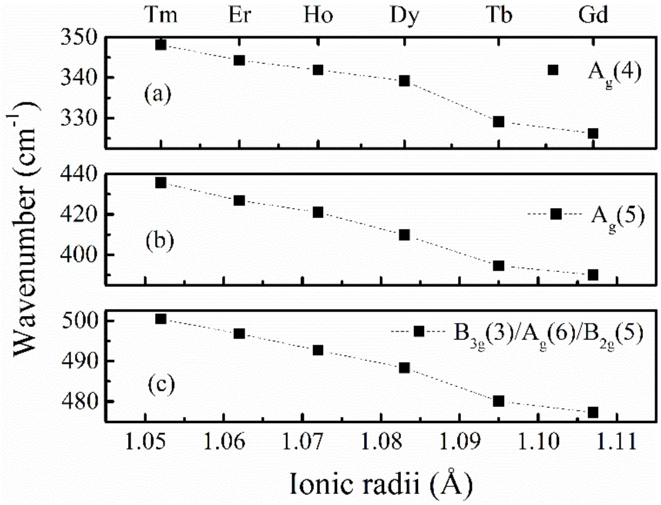

Figure 5. Evolution of the room temperature Raman modes′ position with ionic radii of R^{3+} in $RCrO_3$.

Table 7. Raman shifts of different modes.

Sample	**$B_{2g}(2)$ (cm^{-1})**	**$A_g(3)$ (cm^{-1})**	**$A_g(4)$ (cm^{-1})**	**$A_g(5)$ (cm^{-1})**	**$B_{3g}(3)/A_g(6)/B_{2g}(5)$ (cm^{-1})**
GCO	160.243	254.964	326.219	390.039	477.263
TbCO	157.887	259.610	329.099	394.616	480.094
DCO	162.914	266.324	339.219	409.809	488.344
HCO	162.137	274.266	341.914	421.049	492.693
ECO	161.086	274.968	344.338	426.876	496.775
TmCO	161.354	280.455	348.055	435.690	500.429

3.3 Optic and Electronic Properties

The UV–Vis diffuse reflectance spectroscopy was used to probe the electronic behaviors present in the $RCrO_3$, such as electronic transitions of the different orbitals of a solid.[42] The reflectance spectra is plotted in Fig. 6(a). To determine the bandgap, the measured reflectance (R) needs to be converted to its corresponding absorption (F_R) according to the Kubelka–Munk function:[42]

$$F_R = \frac{(1-R)^2}{2R} \tag{1}$$

In order to calculate the bandgap, Tauc's equation is employed as below:[43]

$$\alpha h v = B(hv - E_g)^n \tag{2}$$

Here α is the optical absorption coefficient, h is the Planck constant, v is the photon's frequency, B is a characteristic parameter, E_g is the energy bandgap, and n is the 1/2 for a direct allowed transition. Here F_R has been put into Eq. (2) as α.[43] Based on Eq. (2), the plot of $(\alpha hv)^2$ versus hv is presented in Fig. 6(b). For the determination of optical bandgap, a representative case of HCO is demonstrated separately in Fig. 6(c). The region with a linear increase with increasing energy in Tauc plot is characteristic of the semiconductor materials and can be linearly fitted. The estimation of bandgap can thus be obtained by the extrapolation of the linear fit and the point of intersection on the x-axis and is shown as purple solid line in Fig. 6(c). The experimental optical bandgaps thus obtained for all $RCrO_3$ are tabulated in Table 8. It can be noticed that the bandgap for GCO, TbCO, DCO, HCO, ECO, and TmCO is 3.21, 3.27, 3.28, 3.29, 3.28, and 3.29 eV, respectively. These observed values of bandgap are close to some of the reported bandgap of $RCrO_3$.[17] This wide bandgap (~3.3eV) of the present $RCrO_3$ can be possibly attributed to the charge transfer gap of O^{2-} $2p$ -Cr^{3+} $3d(t_{2g})$.[17,44]

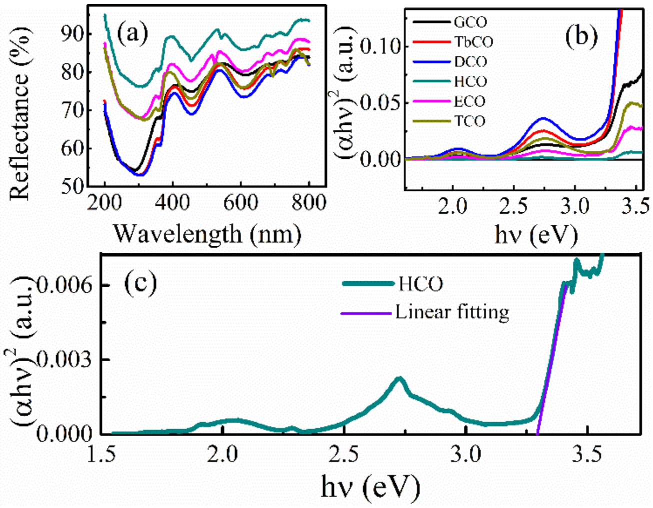

Figure 6. (a) The UV-Vis diffuse reflectance spectra and (b) optical absorption plots $(\alpha h\nu)^2$ of rare-earth chromites. (c) optical absorption edge of $HoCrO_3$.

The first principles calculations were also carried out to understand the electronic and optical properties of $RCrO_3$. We have calculated the bandgaps for the $RCrO_3$ using the *spin polarized* PBE+U and SCAN+U with VASP. Fig. 7 presents the band structures of $RCrO_3$ materials calculated by PBE+U (for spin up [Fig. 7(a)] and spin down [Fig. 7(b)]) where the top of valence band is set to be zero (Fermi level, E_F) for convenience. It can be seen that all the members of $RCrO_3$ studied here exhibit very similar band structure. It is also observed that $RCrO_3$ is an indirect gap semiconductor since the highest occupied orbitals and the minimum of the lowest unoccupied orbitals occur at the point S and Γ, respectively. The density of states (DOS) of all $RCrO_3$ materials is plotted as a function of energy in Fig. 8(a) that exhibits similar energy gap for all with a value around 2.6 eV (also listed in Table 8). This bandgap value for $RCrO_3$ is lower than the experimentally obtained values mentioned above. This is expected as the GGA-PBE always underestimates the electronic bandgap.[45] In the vicinity of E_F (- 3 eV – 0 eV) of the valence band of GCO, the majority of the DOS arises from the *d* states of Cr and *p* states of O.[29] The bottom of the conduction band is composed of O 2*p* and Cr 3*d* orbitals, but is mainly dominated by Cr 3*d* orbitals. Therefore, the observed optical transition originates from O 2*p* orbitals of valence band to Cr 3*d* orbitals of conduction band.

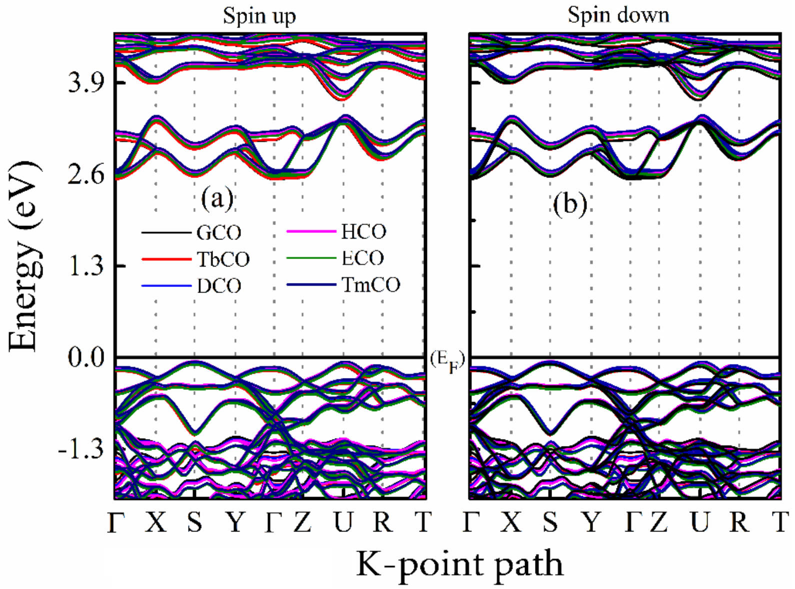

Figure 7. Band structure of $RCrO_3$ calculated by PBE+U simulation, (a) up-spins and (b) down-spins. The top of valence band is set to be zero (Fermi level, E_F).

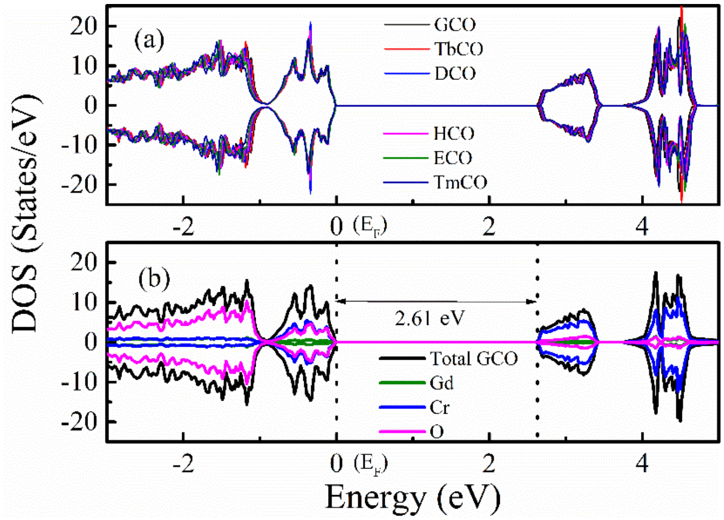

Figure 8. (a) Calculated total density of states (DOS) for $RCrO_3$ by the PBE+U simulation. (b) Calculated total and atom projected DOS of $GdCrO_3$ by the PBE+U simulation. The top of valence band is set to be zero (Fermi level, E_F).

Here, we have proposed the SCAN functional to calculate the band structure of $RCrO_3$, as SCAN is proved to be better than the PBE version of the GGA exchange correlation functional in reproducing accurate and correct ground-state structures of several other compounds.[46] However, SCAN functional also requires a Hubbard U correction to reproduce the ground-state lattice parameters, magnetic moments, and electronic properties of several materials such as Ce-, Mn-, and Fe-based oxides.[46] To explore whether SCAN+U scheme can give a reasonably accurate description of the electronic structure of the $RCrO_3$ material, the DFT calculations for two representative $RCrO_3$ ($GdCrO_3$ and $DyCrO_3$) were performed with a series of U values assigned to *4f* and *3d* orbitals. Fig. 9 displays the variation of total and projected DOS of $GdCrO_3$ with the Hubbard-U ranging from 0 to 3 eV and 0 to 4.6 eV for Cr and Gd, respectively. Firstly, without accounting for the on-site Coulomb repulsion among the *3d* and *4f* electrons (U = 0 eV), a bandgap of 2.60 eV is observed and the *4f* states are delocalized within the O *2p* band. By introducing the on-site Hubbard repulsion upon *3d* states (U= 3 eV for Cr), the bandgap is increased and the *4f* states still resides within the O *2p* band. Intriguingly, when the on-site repulsion among *4f* electrons was taken into consideration, the separation of *4f* states gradually increases with the increasing U value of Gd (due to stronger orbital repulsion). However, the bandgap does not increase with the increasing Hubbard-U value on *4f* indicating that the bandgap is principally determined by the position of conduction *3d* and valence *2p* states in $GdCrO_3$. Finally, when the U value for Gd increases to the suggested value of 4.6 eV in ref.[34][34], a gap opens between the Gd *4f* and O *2p* bands and the *4f* bands locate approximately 5 eV below the E_F. In the case of $DyCrO_3$, SCAN alone tends to underestimate the bandgap and place *f*-states close to the E_F as shown in Fig. 10 (a). With the introduction of a U correction of 5 eV for Dy, a gap opens up between the *4f* states and *2p* states as depicted in Fig. 10 (b). The variation of *4f* electronic structures of the two materials under different U values agrees with the previous viewpoint that proper Hubbard U values are required to place *f*-states in positions like those produced by the hybrid functional.[34] Therefore, the U values suggested by Topsakal *et al*. are employed as the Hubbard U parameter for *4f* orbitals of rare-earth ions in the subsequent calculations.[34]

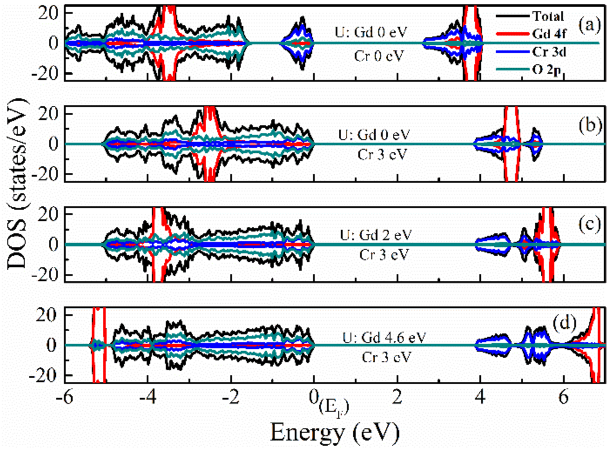

Figure 9. Calculated total and projected density of states (DOS) of GdCrO$_3$ by the SCAN+U simulation with a series of U trials. The Hubbard U corrections for Gd and Cr are: (a) 0 eV and 0 eV, (b) 0 eV and 3 eV, (c) 2 eV and 3e V, and (d) 4.6 eV and 3 eV, respectively. This figure shows how the bandgap is affected by the chosen U values and the resulting orbital repulsions.

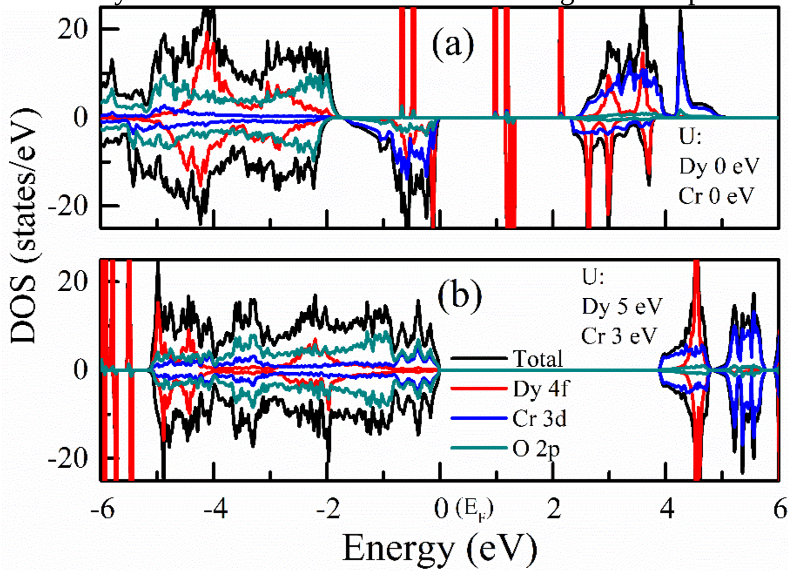

Figure 10. Calculated total and projected density of states (DOS) of DyCrO$_3$ by the SCAN+U simulation with Hubbard U corrections for Dy and Cr as: (a) 0 eV and 0 eV and (b) 5 eV and 3 eV, respectively. This figure also shows how the U parameter affects the orbital repulsions and bandgaps.

The band structures of RCrO$_3$ and their corresponding total and projected DOS are calculated within the SCAN+U scheme and plotted in Fig. 11 and 12, respectively. The band structure shown in Fig. 11 also confirms that RCrO$_3$ materials studied here are indirect bandgap semiconductors, for the valence band maximum (VBM) at S and the conduction band minimum (CBM) at Γ. Fig. 12 shows the density of spin-up and spin-down states of RCrO$_3$ both behaving as semiconductor, consistent with previous band structure calculations in Fig. 11. The contribution from R *4f*, Cr 3*d* and O 2*p* states to the total DOS have been explicitly plotted and used to determine the type of bandgap. The top of the valence band shows an O 2*p* character, while the bottom of the conduction band has a Cr 3*d* character.[47] The contribution from O 2*p* state dominates in the energy range below Fermi level, while the Cr 3*d* state contribution more above Fermi level in the conduction band. The contribution from R *4f* crossing the E$_F$ is negligible when compared to the contribution from Cr 3*d* and O 2*p* states. According to the charge-transfer (CT) energy required to move an electron from the anion valence band to the *d* orbitals at the transition-metal site, $RCrO_3$ can be classified as CT semiconductors with a *p* – *d* type gap between the O^{2-} 2*p* filled band and the Cr^{3+} 3*d* upper Hubbard band.[48] The bandgaps of GCO, TbCO, DCO, HCO, ECO, and TmCO are estimated to be 3.46 eV, 2.92 eV, 3.43 eV, 3.53 eV, 3.44 eV, and 3.52 eV from Fig. 12, respectively, as listed in Table 8. Obviously, the present energy gap is wider than the experimentally obtained energy-gap value of ~3.2 eV, and also wider than another calculation result of ~2.7 eV by PBE+U. The calculated results clearly indicate that the SCAN+U could reproduce the Cr 3*d* and O 2*p* bands crossing the Fermi level more correctly than that by PBE+U.

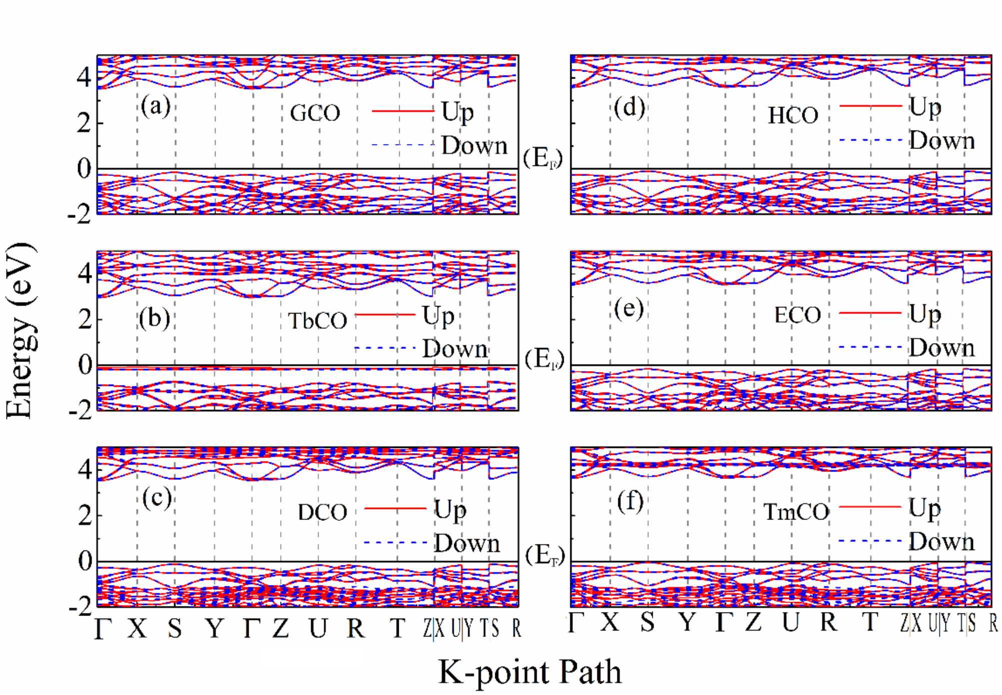

Figure 11. Calculated band structure by SCAN with Hubbard U correction, (a) $GdCrO_3$, (b) $TbCrO_3$, (c) $DyCrO_3$, (d) $HoCrO_3$, (e) $ErCrO_3$, (f) $TmCrO_3$. The top of valence band is set to be zero (Fermi level, E_F).

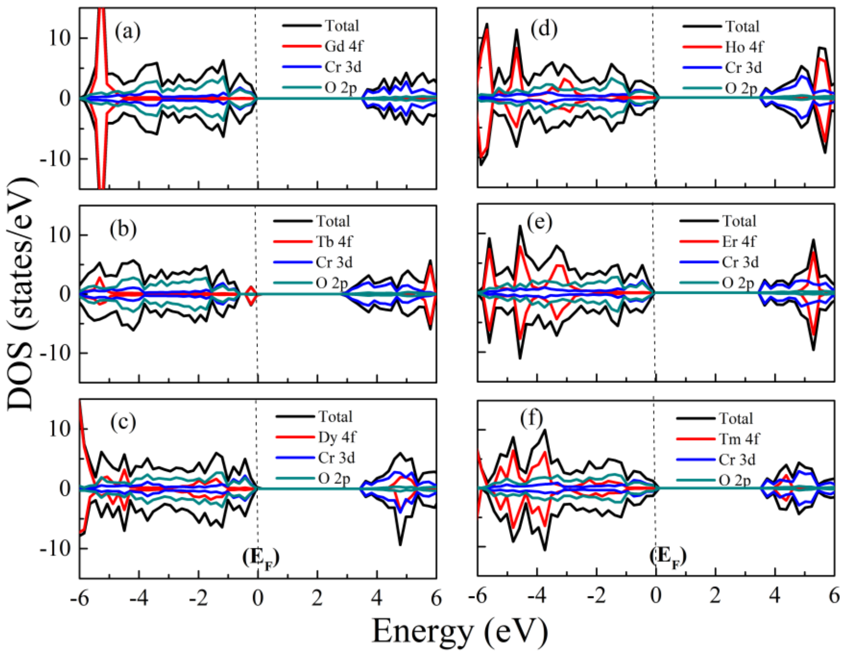

Figure 12. The calculated and atom projected density of states (DOS) by SCAN+U simulation. (a) $GdCrO_3$, (b) $TbCrO_3$, (c) $DyCrO_3$, (d) $HoCrO_3$, (e) $ErCrO_3$, (f) $TmCrO_3$. The top of valence band is set to be zero (Fermi level, E_F).

Table 8. Bandgap of $RCrO_3$ obtained from the Tauc plot (experimental) and DFT (PBE+U, SCAN+U) calculations.

Sample	**Experimental (eV)**	**DFT (PBE+U) (eV)**	**DFT (SCAN+U) (eV)**
GCO	3.21	2.61	3.46
TbCO	3.27	2.62	2.92
DCO	3.28	2.63	3.43
HCO	3.29	2.65	3.53
ECO	3.28	2.66	3.44
TmCO	3.29	2.66	3.52

4. Conclusions

A comprehensive study in terms of structural, optical, and electronic properties of $RCrO_3$ (R=Gd, Tb, Dy, Ho, Er, and Tm) has been carried out on all the samples both experimentally and theoretically by first-principles density functional theory (DFT). Bandgap and structural distortions of $RCrO_3$ in terms of Cr-O-Cr bond angles, unit cell volume, and lattice parameters have been experimentally determined from the UV-Vis spectra and Rietveld refinement of the x-ray diffraction (XRD) scans, respectively. The lattice parameters *a* and *c* were found to consistently reduce with decreasing ionic radii of R^{3+} ion. Raman modes, such as $A_g(3)$ and $A_g(5)$, shifted to lower wave numbers with increasing ionic radii of R^{3+}, indicating a consistent structural distortion associated with octahedral rotation. The optical bandgap of $RCrO_3$ revealed by UV-Vis spectra was ~3.3 eV. We also evaluated the performance of generalized gradient approximation (PBE) and meta-GGA (SCAN) functional with Hubbard U correction for predicting the structural and electronic properties in these perovskite-type $RCrO_3$. The severe crystal distortion with smaller R^{3+} ionic radius was also revealed by both PBE+U and SCAN+U DFT simulations, which agrees with the results obtained from XRD and Raman spectra. It was found that the SCAN+U framework could reproduce a more accurate ground-state crystal structure than that predicted by PBE+U. The bandgap of $RCrO_3$ predicted by SCAN+U simulation (~3.4 eV) is closer to the bandgap (~3.3 eV) determined experimentally, while the bandgap calculated by PBE+U (~ 2.6 eV) differs from experimental values. Thus, in this study SCAN+U is shown to be superior to PBE+U in predicting both the structural properties and band structure of $RCrO_3$.

Acknowledgements:

Author MJ acknowledges UConn Institute of Materials Science - Interdisciplinary Multi-Investigator Materials Program (IMS-IMMP) as well as UConn - College of Liberal Arts and Sciences for financial support for this research. The VASP calculations were performed using the ab-initio total-energy and molecular dynamics program developed at the Fakultät für Physik of the Universität Wien,[31,32] under a software license agreement between GWF's research group at UConn and the Universität Wien. We also acknowledge the computing resources provided by the Center for Functional Nanomaterials, which is a U.S. DOE Office of Science Facility, at Brookhaven National Laboratory under Contract No. DE-SC0012704. SLS thanks the US Department of Energy, Office of Basic Energy Sciences, Division of Chemical, Biological and Geological Sciences under grant DE-FG02-86ER13622 for support of this research.

References

[1] L. Yin, J. Yang, P. Tong, X. Luo, C. Park, K. Shin, W. Song, J. Dai, K. Kim, and X. Zhu, Role of rare earth ions in the magnetic, magnetocaloric and magnetoelectric properties of $RCrO_3$ (R= Dy, Nd, Tb, Er) crystals, J. Mater. Chem. C . **4**, 11198 (2016).

[2] H. Yamamoto, S. Okamoto, and H. Kobayashi, Luminescence of rare-earth ions in perovskite-type oxides: from basic research to applications, J. Lumin. **100**, 325 (2002).

[3] M. K. Warshi, V. Mishra, A. Sagdeo, V. Mishra, R. Kumar, and P. Sagdeo, Structural, optical and electronic properties of $RFeO_3$, Ceram. Int. **44**, 8344 (2018).

[4] Y. Ye, A. Cui, M. Bian, K. Jiang, L. Zhu, J. Zhang, L. Shang, Y. Li, Z. Hu, and J. Chu, Temperature and pressure manipulation of magnetic ordering and phonon dynamics with phase transition in multiferroic GdFeO 3: Evidence from Raman scattering, Phys. Rev. B **102**, 024103 (2020).

[5] A. Akbashev, A. Semisalova, N. Perov, and A. Kaul, Weak ferromagnetism in hexagonal orthoferrites RFeO3 (R= Lu, Er-Tb), Appl. Phys. Lett. **99**, 122502 (2011).

[6] Y. Tokura and Y. Tomioka, Colossal magnetoresistive manganites, J. Magn. Magn. Mater. **200**, 1 (1999).

[7] D. V. Efremov, J. Van Den Brink, and D. I. Khomskii, Bond-versus site-centred ordering and possible ferroelectricity in manganites, Nat. Mater. **3**, 853 (2004).

[8] T. Goto, T. Kimura, G. Lawes, A. Ramirez, and Y. Tokura, Ferroelectricity and giant magnetocapacitance in perovskite rare-earth manganites, Phys. Rev. Lett. **92**, 257201 (2004).

[9] G. Giovannetti, S. Kumar, D. Khomskii, S. Picozzi, and J. van den Brink, Multiferroicity in Rare-Earth Nickelates R NiO_3, Phys. Rev. Lett. **103**, 156401 (2009).

[10] S. Catalano, M. Gibert, J. Fowlie, J. Iniguez, J.-M. Triscone, and J. Kreisel, Rare-earth nickelates $RNiO_3$: thin films and heterostructures, Rep. Prog. Phys. **81**, 046501 (2018).

[11] J. Varignon, M. N. Grisolia, J. Íñiguez, A. Barthélémy, and M. Bibes, Complete phase diagram of rare-earth nickelates from first-principles, npj Quantum Mater. **2**, 1 (2017).

[12] J. R. Sahu, C. R. Serrao, N. Ray, U. V. Waghmare, and C. Rao, Rare earth chromites: a new family of multiferroics, J. Mater. Chem. **17**, 42 (2007).

[13] R. Saha, A. Sundaresan, and C. Rao, Novel features of multiferroic and magnetoelectric ferrites and chromites exhibiting magnetically driven ferroelectricity, Mater. Horiz. **1**, 20 (2014).

[14] G. S. Rao, B. Wanklyn, and C. Rao, Solid State Chemistry: Selected Papers of CNR Rao, World Sci. **4**, 365(1995).

[15] J. s. Prado-Gonjal, R. Schmidt, J.-J. Romero, D. Ávila, U. Amador, and E. Morán, Microwave-assisted synthesis, microstructure, and physical properties of rare-earth chromites, Inorg. Chem. **52**, 313 (2013).

[16] K. D. Singh, F. Singh, R. Choudhary, and R. Kumar, Consequences of R^{3+} cationic radii on the dielectric and magnetic behavior of R CrO_3 perovskites, Appl. Phys. A **126**, 1 (2020).

[17] K. D. Singh, R. Pandit, and R. Kumar, Effect of rare earth ions on structural and optical properties of specific perovskite orthochromates; $RCrO_3$ (R= La, Nd, Eu, Gd, Dy, and Y), Solid State Sci. **85**, 70 (2018).

[18] G. Oliveira, A. Pires, P. Machado, A. Pereira, J. Araújo, and A. Lopes, Effect of chemical pressure on the magnetocaloric effect of perovskite-like $RCrO_3$ (R-Yb, Er, Sm and Y), J. Alloys Compd. **797**, 269 (2019).

[19] S. Mahana, U. Manju, P. Nandi, E. Welter, K. Priolkar, and D. Topwal, Role of local structural distortion in driving ferroelectricity in $GdCrO_3$, Phys. Rev. B **97**, 224107 (2018).

[20] H. J. Zhao, L. Bellaiche, X. M. Chen, and J. Íñiguez, Improper electric polarization in simple perovskite oxides with two magnetic sublattices, Nat. Commun. **8**, 1 (2017).

[21] J. H. Yang, D. A. Kitchaev, and G. Ceder, Rationalizing accurate structure prediction in the meta-GGA SCAN functional, Phys. Rev. B **100**, 035132 (2019).

[22] R. Godby, M. Schlüter, and L. Sham, Accurate exchange-correlation potential for silicon and its discontinuity on addition of an electron, Phys. Rev. Lett. **56**, 2415 (1986).

[23] K. Terakura, T. Oguchi, A. Williams, and J. Kübler, Band theory of insulating transition-metal monoxides: Band-structure calculations, Phys. Rev. B **30**, 4734 (1984).

[24] R. Albers, N. E. Christensen, and A. Svane, Hubbard-U band-structure methods, J. Phys. Condens. Matter. **21**, 343201 (2009).

[25] B. Himmetoglu, A. Floris, S. De Gironcoli, and M. Cococcioni, Hubbard ‐ corrected DFT energy functionals: The LDA+ U description of correlated systems, Int. J. Quantum Chem. **114**, 14 (2014).

[26] M. Staruch, V. Sharma, C. dela Cruz, R. Ramprasad, and M. Jain, Magnetic ordering in TbMn0. 5Cr0. 5O3 studied by neutron diffraction and first-principles calculations, J. Appl. Phys. **116**, 033919 (2014).

[27] S. Terkhi, S. Bentata, Z. Aziz, T. Lantri, and B. Abbar, First principle calculations of structural, electronic and magnetic properties of cubic $GdCrO_3$ Perovskite, Indian J. Phys. **92**, 847 (2018).

[28] S. Terkhi, R. Bentata, F. Bendahma, T. Lantri, S. Bentata, Z. Aziz, and B. Abbar, Half-metallic ferromagnetic behavior of cubic lanthanide based on perovskite-type oxide $NdCrO_3$: first-principles calculations, Indian J. Phys. **95**, 833 (2021).

[29] S. Yin, V. Sharma, A. McDannald, F. A. Reboredo, and M. Jain, Magnetic and magnetocaloric properties of iron substituted holmium chromite and dysprosium chromite, RSC Adv. **6**, 9475 (2016).

[30] K. P. Ong, P. Blaha, and P. Wu, Origin of the light green color and electronic ground state of LaCr O_3, Phys. Rev. B **77**, 073102 (2008).

[31] G. Kresse and J. Furthmüller, Efficient iterative schemes for ab initio total-energy calculations using a plane-wave basis set, Phys. Rev. B **54**, 11169 (1996).

[32] G. Kresse and D. Joubert, From ultrasoft pseudopotentials to the projector augmented-wave method, Phys. Rev. B **59**, 1758 (1999).

[33] I.-G. Buda, C. Lane, B. Barbiellini, A. Ruzsinszky, J. Sun, and A. Bansil, Characterization of thin film materials using SCAN meta-GGA, an accurate nonempirical density functional, Sci. Rep. **7**, 1 (2017).

[34] M. Topsakal and R. Wentzcovitch, Accurate projected augmented wave (PAW) datasets for rare-earth elements (RE= La–Lu), Comput. Mater. Sci. **95**, 263 (2014).

[35] N. Shamir, H. Shaked, and S. Shtrikman, Magnetic structure of some rare-earth orthochromites, Phys. Rev. B **24**, 6642 (1981).

[36] S. Yuling, J. Zhang, F. Zhenjie, L. Zijiong, S. Yan, and C. Shixun, Magnetic properties of rare earth HoCrO$_3$ chromites, J. Rare Earths **29**, 1060 (2011).

[37] S. Wang, X. Wu, T. Wang, J. Zhang, C. Zhang, L. Yuan, X. Cui, and D. Lu, Mild hydrothermal crystallization of heavy rare-earth chromite RECrO$_3$ (RE= Er, Tm, Yb, Lu) perovskites and magnetic properties, Inorg. Chem. **58**, 2315 (2019).

[38] Y. Zhang, J. Sun, J. P. Perdew, and X. Wu, Comparative first-principles studies of prototypical ferroelectric materials by LDA, GGA, and SCAN meta-GGA, Phys. Rev. B **96**, 035143 (2017).

[39] Y. Jana, J. Saha, and S. Nandi, Assignment of optical phonons at the zone center of distorted orthorhombic RCrO$_3$ (R= La, Pr, Nd, Sm, Eu) perovskites using force-field lattice dynamics model, Vib. Spectrosc. **109**, 103086 (2020).

[40] M. Weber, J. Kreisel, P. Thomas, M. Newton, K. Sardar, and R. Walton, Phonon Raman scattering of RCrO$_3$ perovskites (R= Y, La, Pr, Sm, Gd, Dy, Ho, Yb, Lu), Phys. Rev. B **85**, 054303 (2012).

[41] N. R. Camara, V. Ta Phuoc, I. Monot ‑ Laffez, and M. Zaghrioui, Polarized R aman scattering on single crystals of rare earth orthochromite RCrO$_3$ (R= La, Pr, Nd, and Sm), J Raman Spectrosc. **48**, 1839 (2017).

[42] R. López and R. Gómez, Band-gap energy estimation from diffuse reflectance measurements on sol–gel and commercial TiO$_2$: a comparative study, J. Solgel Sci. Technol. **61**, 1 (2012).

[43] P. Makuła, M. Pacia, and W. Macyk, How to correctly determine the band gap energy of modified semiconductor photocatalysts based on UV–Vis spectra, J. Phys. Chem. Lett. **9**, 6814(2018).

[44] V. R. Mannepalli, M. S. Mohan, and R. Ranjith, Tailoring the bandgap and magnetic properties by bismuth substitution in neodymium chromite, Bull. Mater. Sci. **40**, 1503 (2017).

[45] H. Shaili, E. mehdi Salmani, M. Beraich, R. Essajai, W. Battal, M. Ouafi, A. Elhat, M. Rouchdi, M. h. Taibi, and H. Ez-Zahraouy, Enhanced properties of the chemically prepared Gd-doped SrSnO$_3$ thin films: Experimental and DFT study, Opt. Mater. **107**, 110136 (2020).

[46] O. Y. Long, G. S. Gautam, and E. A. Carter, Evaluating optimal U for 3 d transition-metal oxides within the SCAN+ U framework, Phys. Rev. Mater. **4**, 045401 (2020).

[47] R. Hossain, A. Billah, M. Ishizaki, S. Kubota, F. Hirose, and B. Ahmmad, Oxygen vacancy mediated room-temperature ferromagnetism and bandgap narrowing in DyFe$_{0.5}$Cr$_{0.5}$O$_3$ nanoparticles, Dalton Trans. **50**, 9519 (2021).

[48] Y. Li, Y.-S. Zheng, Y.-A. Zhu, Z.-J. Sui, X.-G. Zhou, D. Chen, and W.-K. Yuan, BEEF-vdW+ U method applied to perovskites: thermodynamic, structural, electronic, and magnetic properties, J. Phys. Condens. Matter. **31**, 145901 (2019).